



RESEARCH ARTICLE

10.1029/2020EA001309

An Array of Low-Cost, High-Speed, Autonomous Electric Field Mills for Thunderstorm Research

Key Points:

- A new electric field instrument is described, including its technical description, theory of operation, data processing, and calibration
- Example data from a network of these instruments deployed in the RELAMPAGO campaign are presented and discussed

Correspondence to:

A. Antunes de Sá,
andre.antunesdesa@colorado.edu

Citation:

Antunes de Sá, A., Marshall, R. A., Sousa, A. P., Viets, A., & Deierling, W. (2020). An array of low-cost, high-speed, autonomous electric field mills for thunderstorm research. *Earth and Space Science*, 7, e2020EA001309. <https://doi.org/10.1029/2020EA001309>

Received 18 JUN 2020

Accepted 25 OCT 2020

Accepted article online 3 NOV 2020

A. Antunes de Sá¹, R. Marshall¹, A. Sousa¹, A. Viets¹, and W. Deierling^{1,2}

¹Smead Aerospace Engineering Sciences Department, University of Colorado Boulder, Boulder, CO, USA, ²National Center for Atmospheric Research, Boulder, CO, USA

Abstract The atmospheric electric field is an important research parameter in understanding storm electrification and energy exchange between lightning and the atmosphere across the globe. The near-surface electric field can range from a few V/m (order of 10–100 V/m), mainly produced by the currents in the global electric circuit and local charge perturbations, to tens of kV/m in the presence of electrified clouds. The electric field mill (EFM), a variable capacitance electrometer, has been the instrument of choice in the atmospheric electricity community studying phenomena associated with the atmospheric electric field. The EFM is particularly useful in following storm movement and evolution, monitoring the fair-weather electric field at distant locations, and measuring the vertical electric field inside clouds with EFM deployments on balloons. In this paper, we describe a new electric field mill ground-based design, which focuses on lowering the manufacturing and operational costs of doing research with an array of EFM instruments while maintaining the scientific capabilities offered by past designs and commercially available devices. The theory of operation, data processing, and calibration of the instrument are also described. Example data from the first generation of these new field mills, deployed in the RELAMPAGO campaign in Argentina, are presented here. The RELAMPAGO deployment and data set illustrate important strengths of this design, for example, cost, autonomy, longevity, and measurement quality.

1. Introduction

An electric field mill (EFM) is a variable capacitance electrometer; that is, it measures the local, ambient in-situ electric field through the charge accumulated on a surface area. Various EFM designs have been developed and documented for over a century (e.g., Bateman et al., 2007; Chalmers, 1967; Chubb, 1990; Harnwell & Voorhis, 1933; Horenstein & Stone, 2001; Malan & Schonland, 1950; Mapleson & Whitlock, 1955; Pellat, 1890; Secker, 1975), and they have been most popularly employed in the atmospheric sciences for studying the quasi-static atmospheric electric field.

The electric field near the Earth's surface in the absence of electrified clouds is maintained by the global electric circuit (GEC) (Liu et al., 2010; Markson, 2007; Roble & Tzur, 1986; Williams & Mareev, 2014), producing a near-surface fair-weather electric field of around ~ 100 V/m. This GEC signal at the surface has been shown to correlate with the global distribution of thunderstorms and electrified clouds, supporting the widespread view that thunderstorms are a major energy input to the GEC (Blakeslee et al., 2014; Liu et al., 2010; Mach et al., 2010, 2011; Whipple, 2007). Originally, the near-surface GEC signal was researched over the oceans where the planetary boundary layer is relatively free of pollution, where the diurnal variation is known as the Carnegie curve after one of the geophysical survey vessel that first measured it (Harrison, 2012). Local perturbations to the GEC signal, especially within the boundary layer, have been discussed and documented (e.g., Anisimov et al., 2017; Lucas et al., 2017; Markson, 2007)

In the presence of electrified clouds, the near-surface electric field is strongly influenced by the cloud's charge regions and lightning neutralization of charges, with fields that can easily increase from a few kV/m to tens of kV/m. EFM measurements of the local electric field can therefore be used to infer the charge distributions dynamically within thunderclouds and provide a better understanding of thundercloud electrification (e.g., Jacobson & Krider, 1976; Koshak & Krider, 1989; 1994; Maier & Krider, 1986; Murphy et al., 1996). Special designs and considerations allow for measurements at altitude on aircraft (Bateman et al., 2007 and references therein), balloons (e.g., Chauzy et al., 1991), and rockets

©2020 The Authors.

This is an open access article under the terms of the Creative Commons Attribution-NonCommercial License, which permits use, distribution and reproduction in any medium, provided the original work is properly cited and is not used for commercial purposes.

(e.g., Winn & Moore, 1971). EFMs can also be used in lightning hazard warning systems for asset protection and safety concerns at airports, golf courses, radio transmission facilities, and so forth (Chubb & Harbour, 2000; Montanya et al., 2004; Murphy et al., 2008), particularly to supplement lightning networks in detecting storms evolving directly overhead.

In this document, we describe an EFM designed at the University of Colorado Boulder (CU Boulder) in the Aerospace Engineering Sciences Department as an efficient solution for EFM array deployments to study the static electric field in electrified thunderclouds and to improve our understanding of electrification processes and lightning physics in conjunction with other relevant atmospheric measurements. While effective EFM solutions exist for atmospheric research, the primary concern of this design is to bring down the cost of doing research with an array of EFM instruments while maintaining their scientific capabilities. The instrument was designed with these requirements in mind:

- measuring electric fields with a dynamic range sufficient to cover both near-surface fair and foul weather electric fields, fast enough to capture charge neutralization due to lightning;
- scalable and cost-effective manufacturing, deployment and operation; and
- autonomous, continuous, and low-power operation for long periods of time (months).

In order to address these requirements and design goals, the main technologies employed in the CU EFM, not seen in other EFM solutions, include the following:

- a novel shaft grounding mechanism, which allows for longer operational time between servicing, faster shaft rotation, and, subsequently, higher measurement bandwidth while simultaneously reducing power consumption induced by frictional sliding mechanisms;
- a novel data processing scheme built around a peak detection algorithm, eliminating the need for a conventional demodulating circuit and allowing the CU EFM to capture field changes nearing the rotation frequency, rather than requiring an integration period of tens to hundreds of rotations; and
- using a GPS-disciplined sampling clock, which allows for sample-accurate comparison of data over a distributed array of EFMs and is essential for phased-array and tomographic science.

An updated version of the design, not described in this manuscript, also includes remote wireless connection via cellular modem, aiding in the cost-effective operation of a distributed EFM array.

This document describes the CU EFM mechanical design, electronics design, and software used to operate it and to process the signal data. A discussion on the instrument calibration procedure and some example data are also provided.

1.1. Background

An EFM operates by moving a grounded shield plate over electrode sense plates, alternately exposing the sense plates to the electric field and then shielding them. This alternation can be continuous, using a grounded spinning rotor (Figure 1), or through back-and-forth actuation. When the sense plates are exposed to the electric field, they collect free electrons according to

$$q(t) = \epsilon_0 EA(t), \quad (1)$$

where $q(t)$ is the time-varying charge accumulation, E is the background electric field, $A(t)$ is the time-varying exposed area of the plates, and ϵ_0 is the permittivity of free space. For a continuous, uniformly spinning rotor, $A(t)$ can be described by a sinusoid as the electrodes are shielded and exposed. Equation 1 then becomes

$$q(t) = \epsilon_0 EA_0 \sin(3\omega t), \quad (2)$$

where A_0 is the nominal area of the set of plates, and ω is the angular velocity of the rotor as it spins over the electrodes. The factor of 3 comes from the fact that there are two groups of three parallel-connected plates in the CU EFM design, and therefore the plates are alternately exposed and shielded three times for every rotation of the motor. Other designs use two or four sets of sense plates, which would modify the equation accordingly.

The effective current induced in the electrodes can be determined by taking the time derivative of Equation 2:

$$I(t) = \epsilon_0 EA_0 3\omega \cos(3\omega t). \quad (3)$$

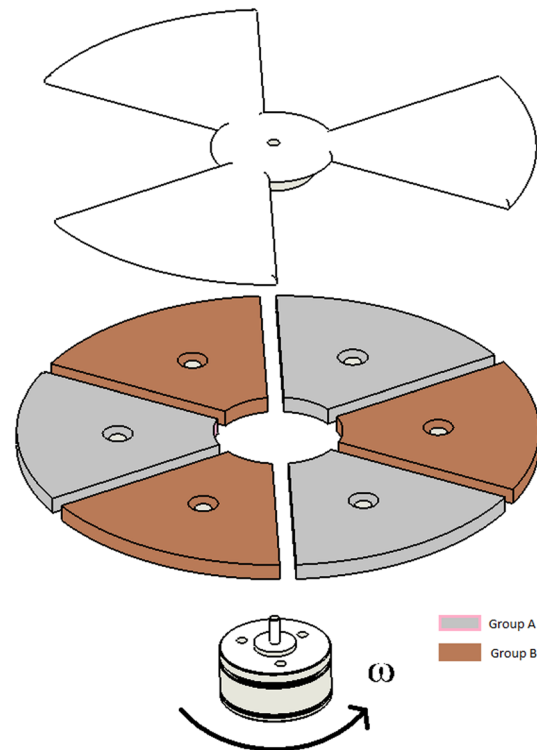


Figure 1. Driving of rotor over plates. The rotor (top) is driven by the motor and grounded; the sense plates are connected in sets of three, noted by the two colored groups.

The ambient electric field, E , assumed to be changing at a rate slower than the rotation of the field mill, is directly proportional to the amplitude of the measured sine wave. The induced currents are then measured with an appropriately designed analog and digital electronics system within a carefully designed structure.

2. System Mechanical Design

The CU EFM instrument consists of several machined aluminum components and makes use of off-the-shelf hardware wherever possible. Several of the components can be manufactured using consumer-grade 3-D printing, such as the LulzBot Taz 6. ABS or similar filament material is required for strength across a wide range of temperatures.

2.1. Mechanical Assembly

Figure 2a shows a blown-up view of the mechanical system. The assembly is comprised of three structural plates—the lid, the top plate, and the bottom plate—separated by standard aluminum standoffs. A 3-D-printed (ABS) holder for the sense plates is placed along the underside of the bottom plate, insulating the electrodes from the grounded aluminum frame. Analog electronics are placed on a custom printed circuit board (PCB) in the lower chamber, while the digital electronics and motor are located on a second PCB in the upper chamber.

The assembly is located within a 15 cm long, 11.5 cm diameter grounded aluminum cylinder, which provides weather protection and electromagnetic shielding, shown in Figure 2b.

2.2. Sense Plates and Rotor

The electrodes consist of six machined aluminum wedges, which rest in an electrically insulating retainer, 3-D printed using ABS. ABS was chosen for ease of manufacturing, replacing a possibly thinner retainer of a material with higher resistivity, such as Kel-F, which is commonly employed in field mill insulation. Each electrode is connected to the analog PCB by a conductive bolt and locking nut. It is important that a robust electrical connection is made; bolts should be chosen to be electrically conductive and noncorroding in an outdoor environment. Figure 2c shows a detail of the electrodes and retainer.

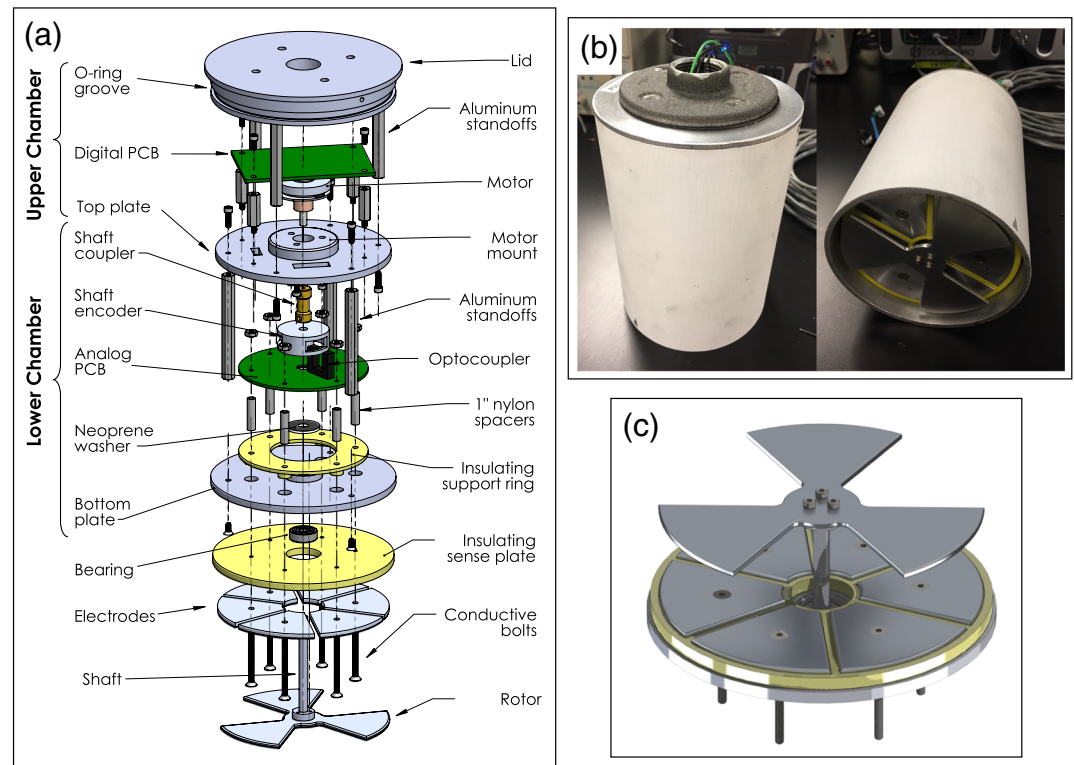


Figure 2. Exploded diagram of the EFM instrument (a), external views of the CU EFM with the aluminum casing (b), and illustration of the sensing electrodes and plastic retaining plate (c).

The rotor is a two-piece design. The rotor blades are machined from a flat aluminum plate, which is bolted onto a cylindrical machined shoulder. The shoulder is then press-fitted onto an aluminum or steel shaft. This design simplifies the machining of the rotor blades and provides excellent perpendicular alignment with the shaft.

2.3. Shaft Grounding System

The rotor and shaft must be kept grounded to prevent bulk charge accumulation, which may introduce erroneous drifts and offsets into the measured signal. Other solutions exist that do not require grounding the shaft (e.g., Chubb, 1990) but introduce more complexity, along with cost and higher power requirements, to the design.

Commercial shaft grounding solutions exist in the form of carbon brush slugs, carbon fiber rings, and metal wire sliding contacts. These devices are designed to prevent electrical discharges through bearings, which can cause pitting and premature wearing. Unfortunately, these solutions introduce substantial mechanical resistance, which greatly increases system power draw, causes mechanical wearing, and reduces the length of time in which the apparatus can operate unattended.

Another possibility, electronic slip rings, which use concentric sets of radial sliding contacts, are used in industrial systems to pass signals along rotating shafts; however, these devices are generally too large and cost-prohibitive for this system.

The CU EFM provides a low-impedance path to ground through the main support bearing. This bearing, a single-shielded NSK 625-Z, was selected through an empirical investigation of deep-groove 625 bearings from several manufacturers. The NSK product is available without grease or preservative wax and provides a reasonably consistent $1\text{ k}\Omega$ path between the rotating and static rings directly from the manufacturer. The bearing is then packed with an electrically conductive carbon grease (MG Chemicals MG-846), which lowers the impedance to under $10\ \Omega$ along a full revolution of the bearing. The bearing is then pressed into the lower aluminum support plate; a neoprene washer is pressed in above to prevent contamination of the grease while allowing for easy servicing. The bearing and assembly are illustrated in Figure 3a.

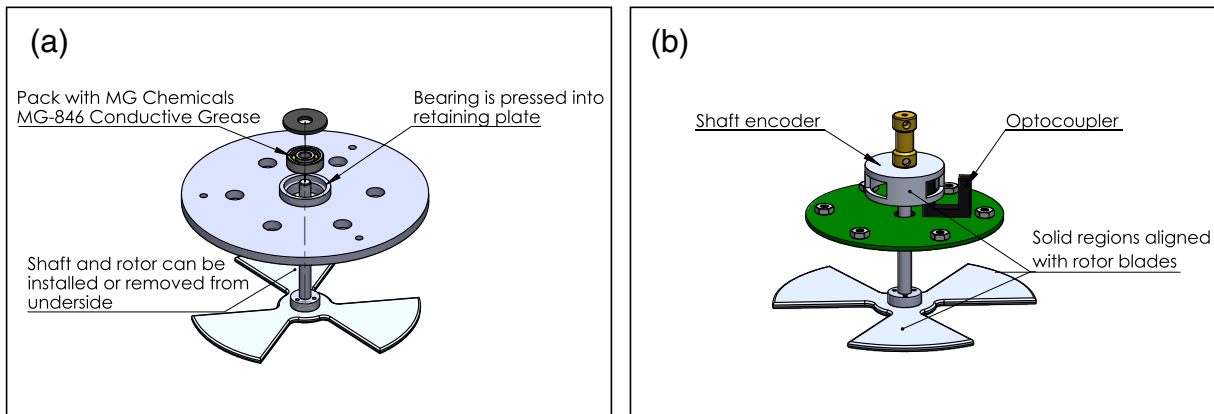


Figure 3. Shaft grounding system (a), composed of a single-shielded 625 bearing packed with conductive grease, and illustration of the optical encoder apparatus (b). Care must be taken to align the encoder with the rotor blades in order to resolve the polarity of the electric field.

3. System Electrical Design

The EFM electrical system consists of two PCBs: (1) an analog board containing signal amplification circuitry and the power supply unit and (2) a digital board containing a microcontroller and peripherals. Figure 4 shows a functional diagram of the two circuit boards. The EFM uses a commercial off-the-shelf Teensy 3.6 microcontroller daughterboard for primary system control and an Adafruit Ultimate GPS module for clock synchronization. The Teensy 3.6 features a 32-bit 180 MHz ARM Cortex-M4 processor, the MK66FX1M0VMD18 by NXP Semiconductors, which has two internal 16-bit successive-approximation (SAR) analog-to-digital converters (ADCs). Most of the EFM signal processing is performed digitally, with the ADCs digitizing the measurement signal early in the processing chain. The digital processing is discussed in the next section.

3.1. Signal Amplification and Conditioning

Figure 5 shows a simplified block diagram of the signal processing chain. Currents induced on both sets of electrodes are amplified via independent transimpedance amplifiers and capacitively coupled to a differential input, variable gain amplifier (VGA), which provides level shifting and adjustable gain. The output is then low-pass filtered to reduce aliasing. The signal is digitized at 16-bit resolution and 1,000 samples per second using the analog-to-digital converter (ADC) onboard the Teensy 3.6 microcontroller. The adjustable gain maps the incoming electric field into the 16-bit ADC, defining the gain, saturation level, and measurement resolution.

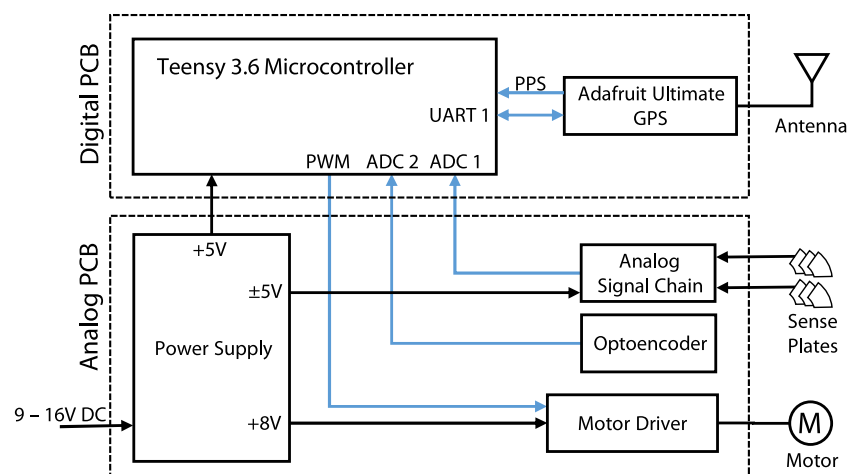


Figure 4. Block diagram of the EFM electrical systems, showing the two PCBs and functional connections.

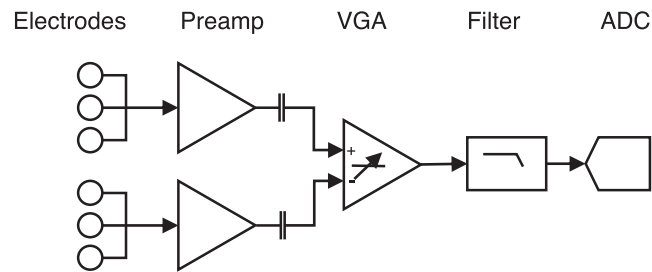


Figure 5. Analog signal preamplification and processing chain.

3.2. Motor Control

Consistent, accurate rotational speed is fundamental to accurately measuring the electric field since the current induced on the electrodes depends on the rotor speed (Equation 3). The EFM uses a three-phase motor (Maxxon EC32, Part No. 339624) and a dedicated motor controller integrated circuit to spin the shaft and grounded rotor. The rotational speed and phase (e.g., which set of sense plates are covered) are measured using a u-shaped optical encoder apparatus, as shown in Figure 3b. The rotational speed is actively managed in software using a PID controller, which is set to 33.3 Hz as the optimal balance between time resolution, power draw, and mechanical longevity. The shaft encoder ring is shimmed or press-fitted onto the shaft. The open and closed sections of the shaft encoder must be aligned with the rotor blades to properly resolve the polarity of the measured electric field. Ideally, the shaft encoder should be machined out of aluminum for durability but may be 3-D-printed using ABS or another high-temperature material and a 100% material fill.

A unique feature of this EFM is that the signal from the optical encoder is directly sampled and recorded by another ADC on the Teensy microcontroller, as opposed to other field mills which perform the phase demodulation with analog electronics (e.g., Bateman et al., 2007). Digitally sampling the phase data has two main advantages: (1) reducing the front-end analog circuitry, which in turn drastically decreases power consumption and signal degradation, and (2) flexibility in the method of phase demodulation done at post-processing and improving robustness over faulty phase data. Because the signal is binary (i.e., either higher or low), we threshold and resample the optical encoder signal to 1 bit to save data volume. The end result is a 1-bit signal (i.e., ones and zeros) at 1,000 samples per second. This digital signal can then be aligned with the electric field signal in postprocessing for recovering the ambient electric field polarity (see section 4).

3.3. Power Supplies

The instrument operates from a nominal 12-volt DC external supply with a power consumption of about 4 W, which can be provided from a battery, solar power system, and/or an AC power adapter. The system is designed to accommodate supplies between 9 and 16 V. One 50 W solar panel and a 100 W hr battery can power the EFM continuously with at least 2 hr of clear-sky sunlight per day, while larger batteries can keep the EFM running for more days without sunlight, and a second panel can be added for ensuring reliability.

Internally, the system operates on three different voltage rails: a +8 V supply, which drives the motor and motor driver; a +5 V supply, which powers the digital systems and sensors; and a bipolar ± 5 V supply for the analog circuitry.

3.4. Data Acquisition and Storage

The Teensy 3.6 microcontroller is set up to use two of its programmable delay block (PDB) channels for triggering the sampling of the two independent 16-bit ADCs. The first ADC samples the conditioned analog signal from the electrodes, which will be later processed into electric field amplitude measurements, while the second ADC samples the optical encoder of the rotor shaft for use in motor speed control and polarity information of the electric field. The PDB channels are programmed to initiate an ADC conversion at the data sampling frequency of 1 kHz. Internal to the ADC peripheral, an ADC conversion consists of acquiring 32 samples of the analog signal, at a faster rate than 1 kHz and with the full 16-bit resolution, and averaging these 32 samples together into the final ADC conversion result.

When an ADC finishes a PDB-triggered conversion, an interrupt service routine (ISR) collects the conversion result of both ADCs onto a buffer (Figure 6). There are two 16 KiB buffers in memory with only one of them actively being filled at any one time. Data from the optical encoder, that is, from the second ADC, are

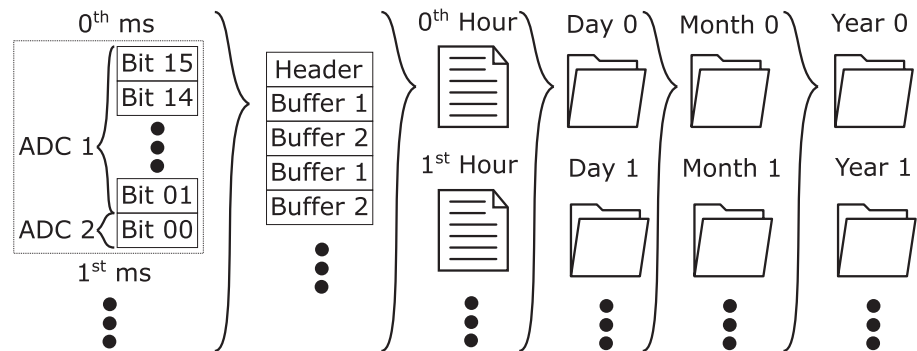


Figure 6. Block diagram of the ADC data storage.

converted into a 1-bit value according to an adaptive threshold and then injected into the least significant bit (LSB) of the conversion result from the first 16-bit ADC. Since the effective number of bits expected for the ADC resolution is about 14 bits (Table 13 NXP Semiconductors, 2017), there is no useful information in the LSB of an ADC reading; additionally, 1-bit information from the optical encoder is enough for extraction of frequency and phase information of the grounded rotor. An adaptive threshold ensures the proper conversion of the optical encoder signal even for different DC biases on the photointerrupter, for example, caused by differing light background levels. The EFM software continuously computes a moving average of the optical encoder signal's low and high values every 100 samples and uses their mean as the threshold. Note that since the rotors turn at 33.3 Hz, one group of three sense electrodes is alternately covered (i.e., optical encoder signal at a lower value) and uncovered (i.e., optical encoder signal at a high value) at 100 Hz, so the 100-sample window for the moving average corresponds to 10 periods of the encoder's sinusoidal signal or about 3.3 rotations of the rotor.

Once a 16 KiB buffer is completely filled, the main code starts the process of writing the filled buffer into a file on the Teensy's SD memory card. The SD card is formatted with a file allocation size of 16 KiB, and thus each buffer copy to the SD card involves only one block write operation, minimizing CPU time.

The ADC data are written to nonvolatile memory through a file hierarchy inside of a FAT32 file system. Each file corresponds to a whole hour of data, which gets stored in parent folders that correspond to the date of the acquired data, that is, day, month, and year folders (Figure 6). Each file also contains a header with the date and hour information for redundancy.

3.5. GPS Timing

Time-tagging of the data is achieved by reading the date-time information output from the Adafruit Ultimate GPS module through a UART line. The internal clock for the CPU, responsible for placing the ADC conversions in their appropriate 1 ms bin, is synchronized in software with the GPS 1 pulse-per-second (PPS) signal, ensuring that the clock error is at most one ADC sample period. With an internal 16 MHz crystal oscillator error of 20 parts per million, the ADC conversion could drift one ADC sample period after every 50 s without the GPS synchronization.

4. Signal Postprocessing

The EFM digitizes the measurement signal early in the processing chain, leaving most of the signal processing to be performed digitally. This design has three major advantages over the use of analog signal processing: (1) It minimizes the analog front-end of the instrument, which translates to cost and power savings; (2) it provides greater accuracy of the electric field solution, as analog signal processing is more susceptible to noise; and (3) it has a flexible design, allowing for easy implementation updates in software. A postprocessing framework, illustrated in Figure 7, is used to convert the raw data saved by the EFM to a calibrated electric field measurement. It can be performed on a conventional computer or in near-real-time in the EFM microcontroller. This unique process involves a series of operations:

1. Hourly data files from the EFM are collected into a single "day" file for processing;
2. The 15-bit data corresponding to the electrode signal (Channel 1) and 1-bit corresponding to the optical encoder signal (Channel 2) are separated;

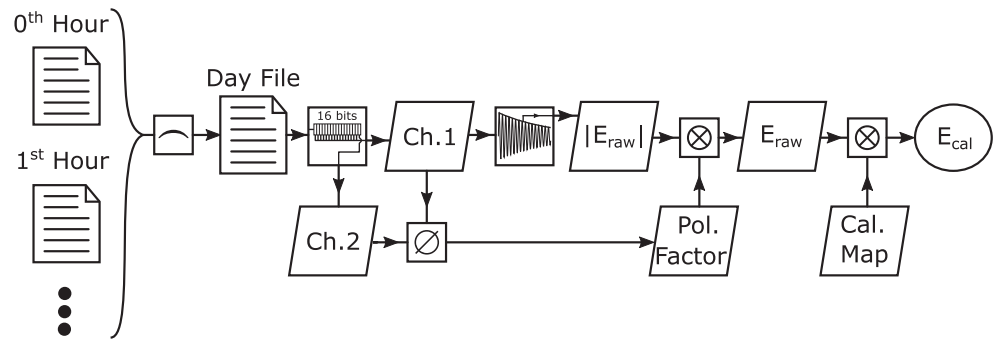


Figure 7. Flowchart summarizing the postprocessing framework for the EFM raw data. The \frown operator indicates a concatenation of data, \emptyset is a binary phase detector, and \otimes indicates a mapping operation. Channel 1 data correspond to the filtered signal at the electrode plates, and Channel 2 corresponds to the optical encoder data.

3. The magnitude of the uncalibrated electric field, $|E_{raw}|$, is computed from the envelope of the Channel 1 signal, as described in section 4.2;
4. The polarity of the signal is found using a binary phase detector and applied to the uncalibrated electric field, as described in section 4.3;
5. A calibration curve is applied to the electric field measurement, yielding the processed calibrated electric field measurements for a given day, described in section 4.4; and
6. The calibrated electric field is decimated to 100 Hz, given the effective time resolution dictated by the rotation speed of the EFM and the number of segments in the rotor.

The theoretical background for the postprocessing is laid out next in section 4.1.

4.1. Theory

At any point in time, the voltage measured at the plates and digitized by the ADC Channel 1, $V(t) = V_0 \cos(3\omega t + \phi)$, is equal to the current induced on the plates, $I(t)$, multiplied by the impedance of the path between the electrodes and ground, $Z_g(3\omega)$. Given that the design includes a path to ground for the electrodes of $1 \text{ M}\Omega$ and that parasitic effects are designed to be negligible, the complex impedance Z_g can be treated as a simple resistance, R . Hence, the phase difference between voltage and current is zero, and the phase, ϕ , is either 0° or 180° depending on the electric field polarity. Rearranging Equation 3 and using the

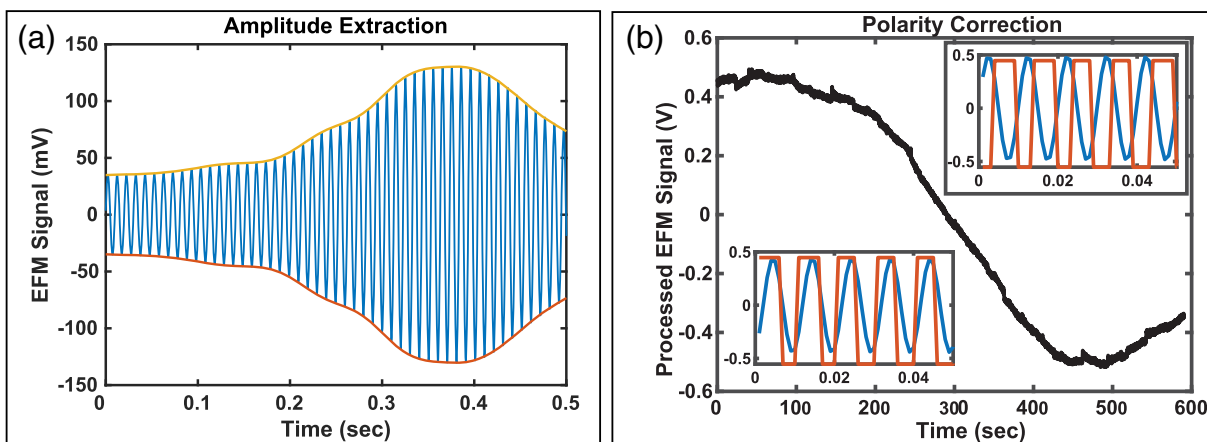


Figure 8. Plot of the digitized voltage readings of the electrode plates (a), $V(t)$, after bandpass filtering, with the extracted amplitude shown in red and yellow, and plot of the postprocessed EFM signal after polarity correction but before the calibration map (b). Two inserts are overlaid on the second plot, displaying the raw (blue) and optical encoder (red) signals under a positive ambient electric field (bottom) and a negative ambient electric field (top).

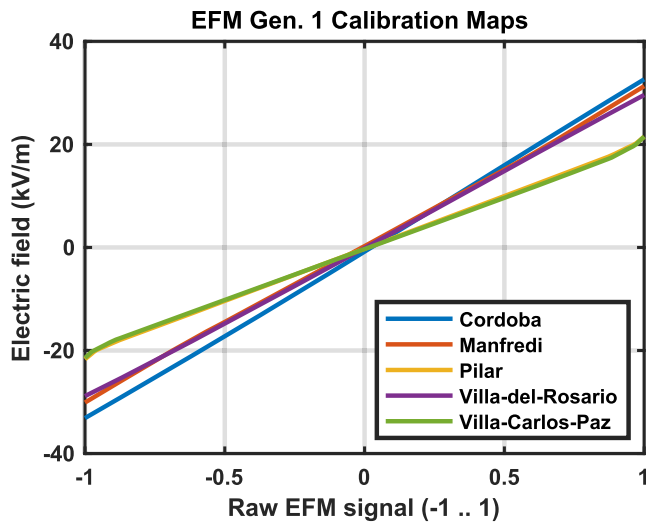


Figure 9. Calibration curves for each site, as computed using the calibration table.

voltage relation above, the magnitude of the ambient electric field can be described as

$$E = \frac{V_0 \cos(3\omega t + \phi)}{R} \frac{\epsilon_0 A_0 3\omega}{\cos(3\omega t)}, \quad (4)$$

$$|E| = \frac{V_0}{R} \epsilon_0 A_0 3\omega = K_f V_0,$$

where V_0 is the instantaneous voltage amplitude of the measured signal, and K_f is a calibration factor that translates the instantaneous voltage into an electric field magnitude.

The sign of the ambient electric field manifests itself as a phase shift of the voltage and current functions with respect to time. The electrode voltage measurement, $V(t)$, by itself, has an absolute phase ambiguity and does not contain enough information for deriving the ambient electric field polarity. In order to solve this ambiguity, a polarity factor, P_f , that changes between ± 1 can be derived from the angular position of the rotor, that is, which set of electrodes is covered (section 4.3).

Even though the calibration factor could be derived directly from the system parameters, that is, ϵ_0 and A_0 , in practice, V_0 depends on many other perturbing variables, such as system noise and various efficiencies, causing distortion of the calibration factor. Thus, a more accurate solution is to employ a calibration curve, $K_m(V_0 P_f)$, to map the amplitude voltage readings into electric field measurements.

Ultimately, the signal postprocessing is performed on a conventional computer, and it involves the extraction of the electrode signal amplitude, V_0 , the computation of the electric field polarity, P_f , and the mapping of the postprocessed signal into an electric field measurement through a calibration map, K_m :

$$E = K_m(V_0 P_f). \quad (5)$$

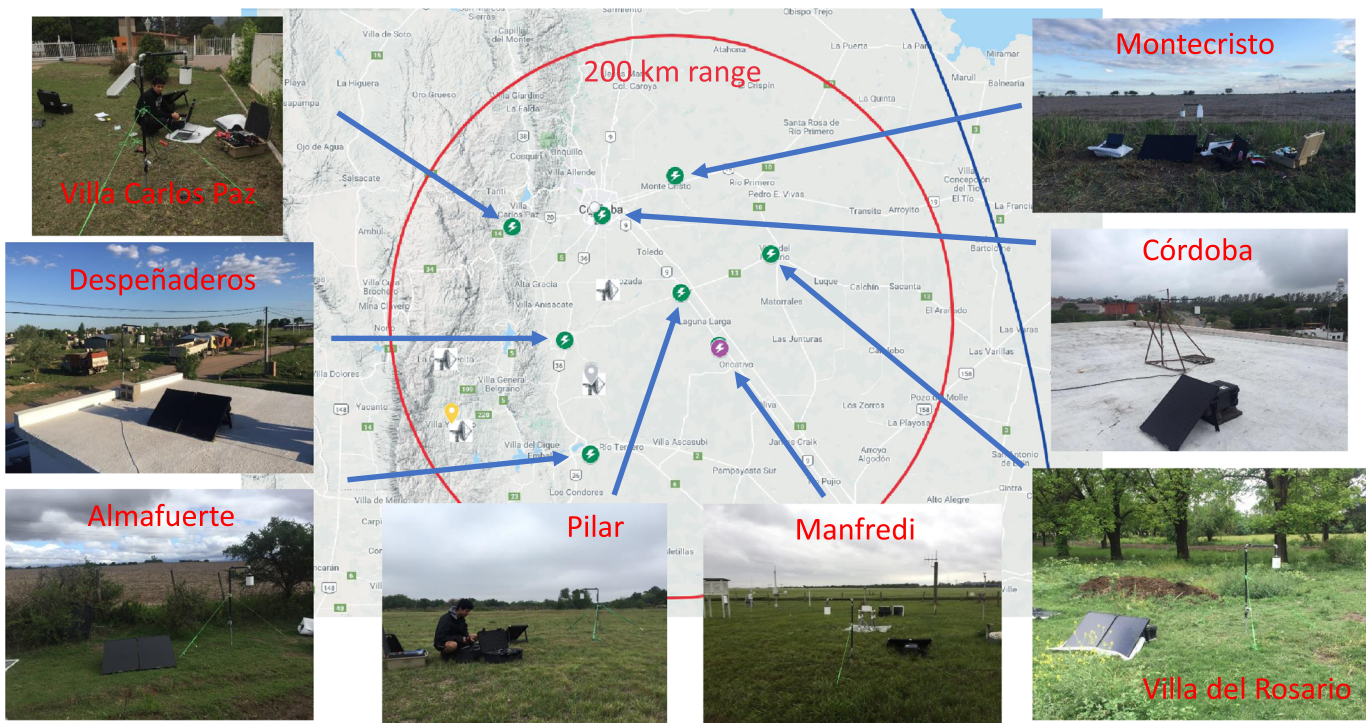


Figure 10. RELAMPAGO site map of the EFM sensors in Argentina.

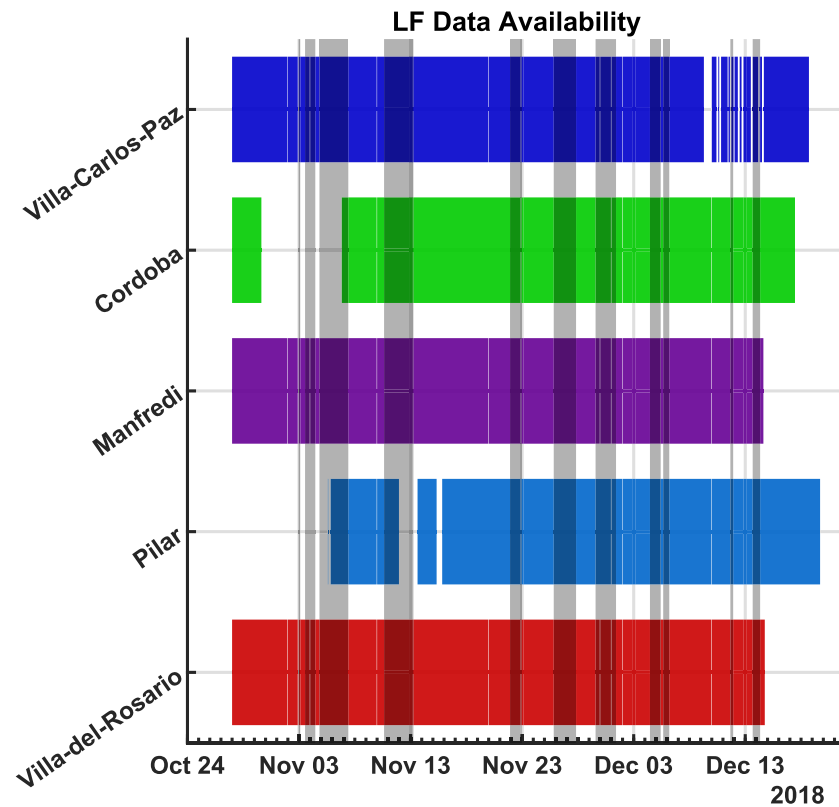


Figure 11. Data coverage during RELAMPAGO for five of the EFMs. Shaded gray regions represent an intensive observing period (IOP) for the campaign.

4.2. Instantaneous Amplitude Extraction

For the amplitude extraction of V_0 from the measured signal $V(t)$, the raw signal is bandpass filtered around the expected signal frequency, thus removing slow linear trends in the data as well as spurious signals not related to the electric field. Once the data are cleaned, the instantaneous amplitude, which is the same as the signal's envelope (Figure 8a), can be extracted using a Hilbert transform (Cizek, 1970) or alternatively using cubic spline interpolation of the wave peaks (de Boor, 1978).

4.3. Polarity Computation

The polarity of the electric field, P_f , is found by comparing the phase of the sinusoid in the raw data against the phase of the optical encoder data, which indicates which set of electrodes was covered by the ground rotor, as seen in the small inserts of Figure 8b showing the raw signal and the optical encoder phase signal when the electric field is positive (left) and negative (right). The optical encoder signal is bandpass filtered and processed through a Hilbert transform in the same manner as the electrode signal. The polarity is then computed by taking the difference between the phase angles of each signal, which yields approximately 0° for in-phase signals and approximately 180° for out-of-phase signals. The result is then thresholded to ± 1 , yielding P_f . The main plot in Figure 8b displays the postprocessed signal after the polarity factor was applied. The peaks and valleys of the raw signal match opposite parts of the phase signal waveform depending on electric field polarity as expected.

4.4. Calibration and Site Correction

Calibration of the EFM is necessary to map the current readings on the electrode plates into a meaningful electric field measurement and also to provide a better understanding of the instrument's linearity and sensitivity not captured in the theoretical electric field measurement equation (Equation 4).

Calibration curves are recorded for an EFM using a calibration table, consisting of two 122 cm parallel metal plates separated by about 30 cm. A hole is cut in the bottom plate to allow the field mill's sensing electrodes to sit flush, mimicking a ground-installed, upward-facing EFM. The plate separation is about 3 times larger

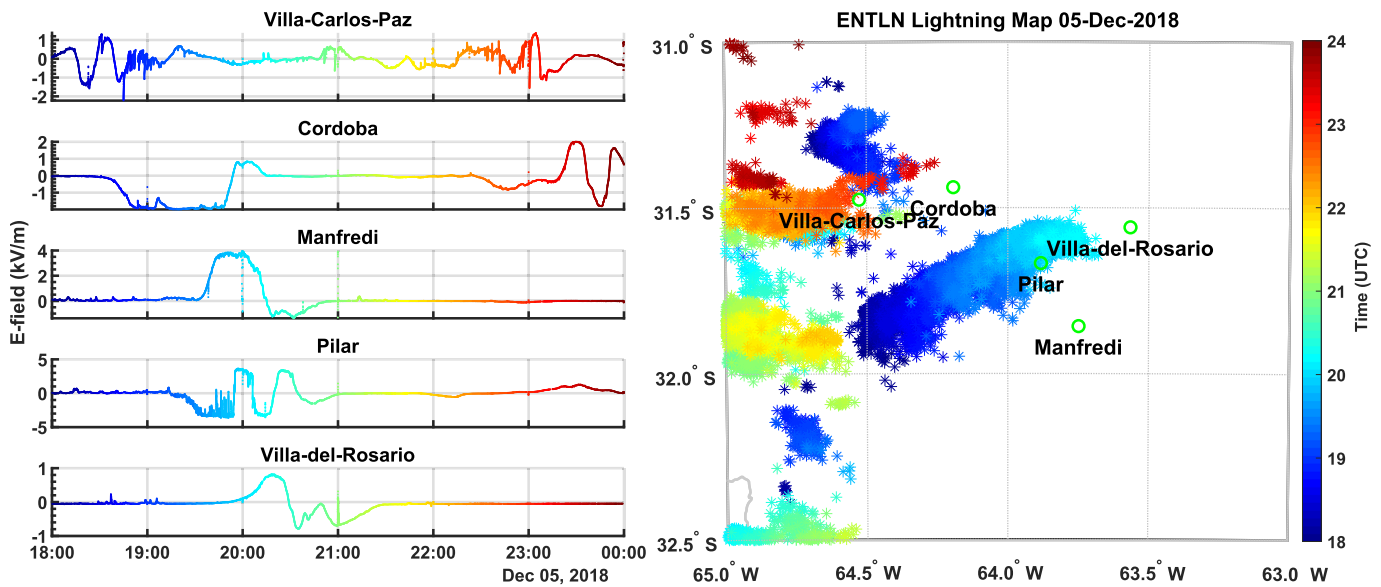


Figure 12. EFM data recorded by different stations during a storm period on 5 December 2018, between 18:00 and 00:00 UTC (left) and lightning map for the storm system, provided by ENTLN (right). The plots are color-coded based on time of day. Both Córdoba and Pilar mills reach their saturation levels.

than the field mill hole, and the plate length is about 2 times larger than the plate separation, following the IEEE standard recommendation (IEEE Standard 1227-1990). The IEEE guidance helps minimize perturbations to the generated electric field at the center and keep its uncertainty below 0.5%. A controlled electric field is induced by applying a voltage across the two plates. A calibration data set is generated with an EFM running, spanning a range of electric fields (Figure 9), which can then be paired with the true electric field measurements to create a calibration map, C_m . The true electric field between the plates can also be measured directly by an independently calibrated electric field instrument, for example, a Campbell Scientific CS-110 EFM, relaxing the design requirements of the calibration table. Our first generation of EFMs deployed (see section 5) were calibrated on the table using the CS-110 as a reference for the relationship between plate voltage and electric field induced.

Figure 9 shows the calibration curves for the first-generation EFMs. Each mill is approximately linear, with some nonlinearities arising at very high electric fields. The difference in sensitivity for each mill, that is, the slope, comes primarily from different electronic gains at the analog amplifier stage, which is adjustable via a trimpot on the first generation EFMs. The gain can be set according to the desired electric field measurement domain. An affine fit to the calibration data reveals a DC offset of ~ 100 V/m, which may drift throughout a 1 month deployment on the order of 100 V/m.

Since the calibration assumes the EFM is mounted flush with the ground, a site correction must be applied to the measured electric field if the mill is mounted in a different configuration, for example, pointing downward, which can greatly reduce its sensitivity, or moving it up from the ground, which can increase its sensitivity. Other smaller perturbations to the instrument gain captured by the site correction include constant systematic effects from the mounting apparatus and site vegetation/topology, such as ground conductivity. An elevated, downward-facing mounting configuration is the most practical for deployment as it avoids particle ingress from the top due to rain or wildlife nesting. Note that the site correction can have a large impact on the instrument sensitivity and must be taken into account when setting the EFM adjustable gain.

The site correction and drift of the calibration DC offset can be modeled with two linear coefficients, C_s and C_{offset} , such that the electric field can be computed as

$$E = K_m(V_0P_f) = C_s C_m(V_0P_f) + C_{\text{offset}}. \quad (6)$$

The site correction and DC offset can be found for any mounted EFM by comparing its measured electric field to a second EFM pointing upward and flush with the ground, and with the reasonable assumption

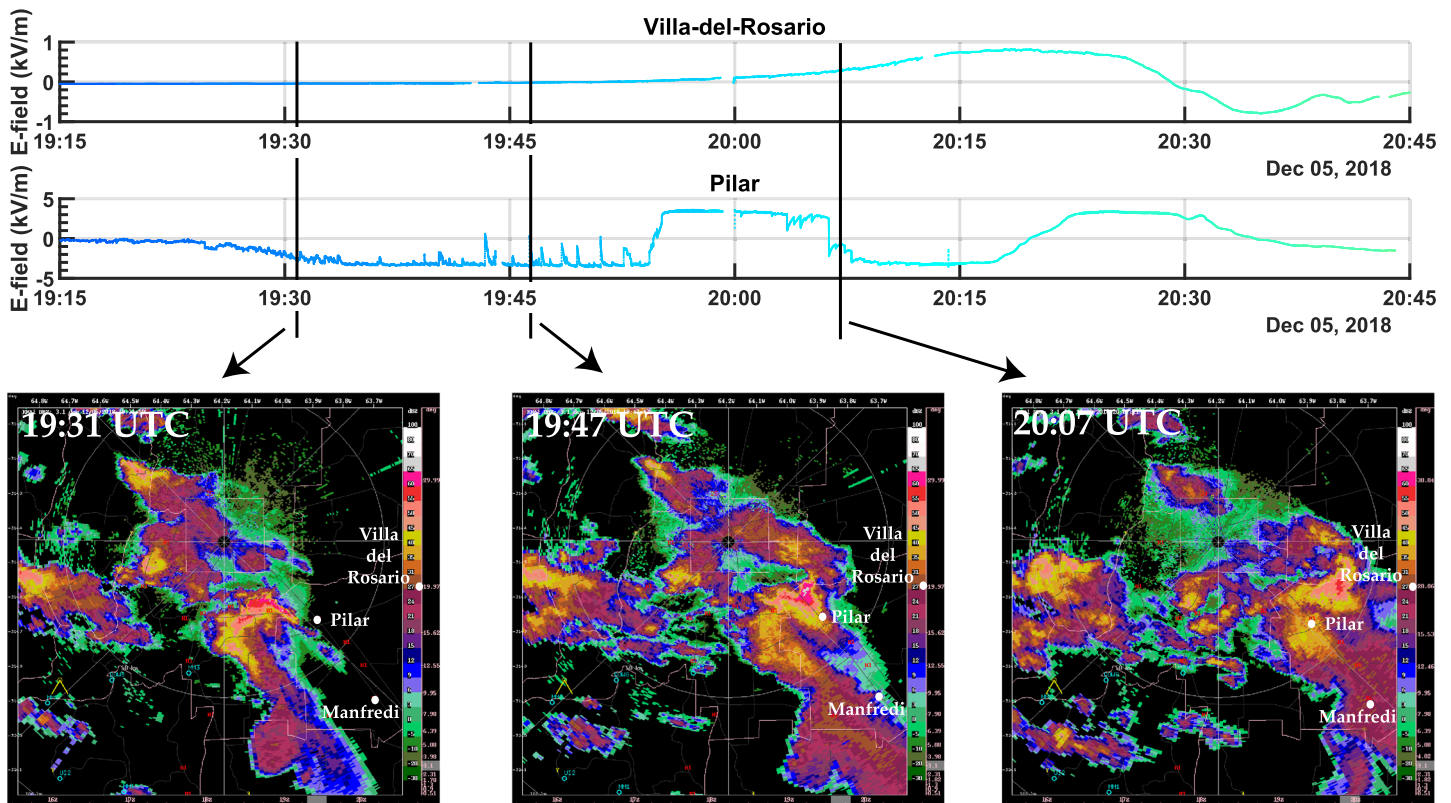


Figure 13. Vertical electric field data recorded by Pilar and Villa del Rosario EFMs during a storm on 5 December 2018 that produced small hail (upper panel). Snapshots of the storm from 3.1° plan position indicator (ppi) scans of radar reflectivity from the Servicio Meteorológico Nacional Córdoba radar are shown in the bottom panels.

that the site correction is constant enough, the determined site correction should be valid through the deployment period.

5. Deployment in Argentina

An array of eight CU EFMs was deployed during the Remote sensing of Electrification, Lightning, And Mesoscale/Microscale Processes with Adaptive Ground Observations (RELAMPAGO) field campaign, conducted between 1 November and 15 December 2018 in west-central Argentina (Nesbitt, 2020). The gain setting on these EFMs, which could not be easily adjusted during deployment, was set too high for the RELAMPAGO storms, leading to saturation during high electric field measurements.

The array of EFMs was deployed to cover the Córdoba region centered around the city of Pilar, as shown in Figure 10.

The deployed EFMs were powered by a 150 W hr battery charged by 100 W solar panels or by wall power in the case of Córdoba and Pilar EFMs. A firmware fault introduced an increasing clock lag to the electric field readings, measured to be on the order of 45 s or an absolute maximum of ~ 70 s before being reset during a clock synchronization to the GPS clock, which occurred every 30 min. The Córdoba EFM ran on an updated firmware and is the only EFM without the mentioned clock lag.

Figure 11 presents the data coverage available from five EFMs in RELAMPAGO, which has been released in the EOL data archive (Deierling et al., 2019). The EFMs were mounted pointing downward, about 1 m above the ground, on a portable steel pipe structure. The field mill was earth grounded by a conducting steel stake driven about 1 ft into the ground at the base of the structure. The correction coefficients, C_s and C_{offset} , were derived from simultaneous measurements of the deployed EFM and a temporary installation of the Campbell Scientific CS-110 on the same steel pipe mounting structure. The CS-110 site correction was acquired by mounting it flush with the ground, and the correction was used at all sites following the assumption that it stayed relatively constant for the same mounting configuration.

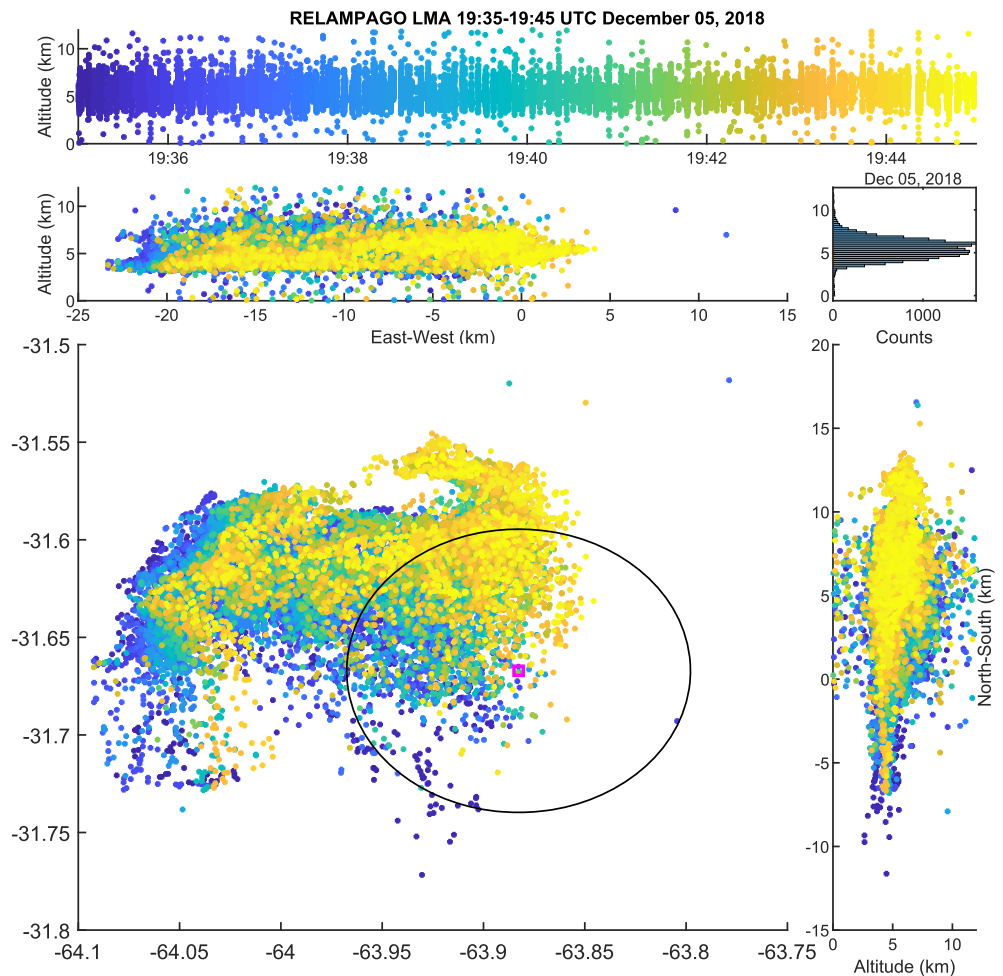


Figure 14. Ten-min LMA VHF radiation sources from 19:45–19:55 UTC of the storm near the Pilar EFM, with a bimodal altitude distribution and a larger number of sources in the lower altitude layer, which might suggest an inverted polarity structure. The colors indicate time progression, and the different panels show the VHF sources height-time (top), plan view (bottom left), and east-west (middle left) and north-south (bottom right) vertical projections. Also shown is a histogram of the source heights.

6. Example Data

During the RELAMPAGO field campaign, surface electric field data were collected for a variety of storms. An example of various storms overhead or in the vicinity of various deployed EFMs on 5 December 2018 is shown in Figure 12, which also shows lightning activity measured by Earth Networks Total Lightning Network (ENTLN). The electric field polarity follows the physics convention, where an electric field pointing toward the Earth is negative. For the period between 18:00 and 24:00 UTC on 5 December 2018, multiple thunderstorm cells moved over the Villa Carlos Paz EFM, which indicates field changes and lightning events. Furthermore, an anomalous charged storm that produced small hail initiated in the southern part of the Sierra de Cordoba's and then moved northeast, skirting Pilar before dissipating just before in Villa-del-Rosario. The Pilar and Villa-del-Rosario EFM captured this storm in its different life stages (Figure 13). Data from the NASA Lightning Mapping Array (LMA), partially shown in Figure 14 for 19:35 to 19:45 UTC, might suggest an inverted polarity charge structure, and the EFM data can be reasonably interpreted within that scenario. The charge structure of RELAMPAGO storms, including the example shown here, is expected to be established in pending publications, and the electric field data will be investigated within the context of storm polarity in future collaborations.

Additionally, a sample period of fair-weather EFM data is shown in Figure 15. It highlights the EFM effective resolution of about 2 V/m for this window, showcasing the instrument's ability to measure fair-weather

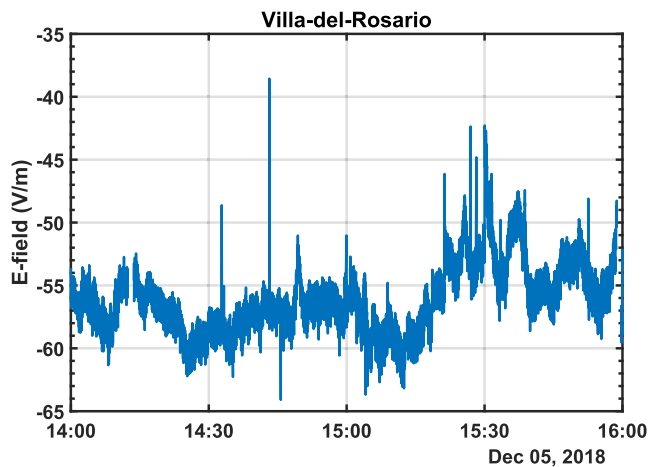


Figure 15. Fair-weather EFM data captured in Villa-del-Rosario for a period of 2 hr from 14–16 UTC, before any storms were present in this area on 5 December 2018.

electric fields at a fast sample rate. Decimating the data from the nominal 100 Hz will allow trading resolution from the time dimension to the electric field measurement. This trade can be used in applications that do not require fast electric field measurements, such as the study of the GEC, where a cadence of 1 Hz for measurements is commonly used. In order to demonstrate the EFM capability of studying fair-weather electric fields, further testing on the EFM sensitivity is needed, in particular with regards to the temperature dependence of the instrument sensitivity and the DC offset drift captured by C_{offset} . Furthermore, the next generation of field mills is designed with an electronic gain solution, providing a more robust solution to the instrument sensitivity and temperature dependence.

7. Summary and Discussion

The mechanical and software design of the CU EFM has been described in this paper, along with an explanation of the instrument theory of operation and data postprocessing. First-generation EFMs, deployed in the RELAMPAGO scientific campaign, prove the EFM design fulfills the original requirements. Electric field measurement highlights presented here show that the CU EFM is capable of measuring foul weather electric

fields and possibly fair-weather fields as well, with lightning signals also observable. The design, even as first-generation, is scalable for large array deployments, allowing for bulk production of machined parts, cost-effective alternative for commercial EFM instruments, and hands-off long-term operation after deployment.

The RELAMPAGO EFM data set is currently being analyzed in conjunction with other campaign instrumentation data to address science questions on thunderstorm electrification, where the EFM data will help provide information on the dynamic charge structure of thunderclouds.

The CU EFM design will continue to be updated as possible improvements to the design are uncovered from the usage of the RELAMPAGO data set. As a cost-effective instrument array solution, the next generation of the CU EFMs will continue to be employed in future research of the atmospheric electric field.

Data Availability Statement

RELAMPAGO EFM, LMA, and radar data sets used for this research are available in these in-text data citation references: Deierling et al. (2019), user agreement required; Lang (2020), user agreement required; and Renolfi et al. (2020), user agreement required. ENTLN data supporting this research are available upon request from Earth Networks (Earth Networks, 2020), under an appropriate license or user agreement, and are not accessible to the public or research community. Earth Networks customer service can be contacted for obtaining licensing or user agreements.

References

- Anisimov, S. V., Galichenko, S. V., Aphinogenov, K. V., & Prokhorchuk, A. A. (2017). Evaluation of the atmospheric boundary-layer electrical variability. *Boundary-Layer Meteorology*, *167*, 327–348. <https://doi.org/10.1007/s10546-017-0328-0>
- Bateman, M. G., Stewart, M. F., Podgorny, S. J., Christian, H. J., Mach, D. M., Blakeslee, R. J., et al. (2007). A low-noise, microprocessor-controlled, internally digitizing rotating-vane electric field mill for airborne platforms. *Journal of Atmospheric and Oceanic Technology*, *24*(7), 1245–1255. <https://doi.org/10.1175/jtech2039.1>
- Blakeslee, R. J., Mach, D. M., Bateman, M. G., & Bailey, J. C. (2014). Seasonal variations in the lightning diurnal cycle and implications for the global electric circuit. *Atmospheric Research*, *135–136*, 228–243. <https://doi.org/10.1016/j.atmosres.2012.09.023>
- Chalmers, J. A. (1967). *Atmospheric electricity* (p. 128). New York: Pergamon Press.
- Chauzy, S., Médale, J.-C., Prieur, S., & Soula, S. (1991). Multilevel measurement of the electric field underneath a thundercloud: 1. A new system and the associated data processing. *Journal of Geophysical Research*, *96*(D12), 22319. <https://doi.org/10.1029/91JD02031>
- Chubb, J. N. (1990). Two new designs of 'field mill' type fieldmeters not requiring earthing of rotating chopper. *IEEE Transactions on Industry Applications*, *26*(6), 1178–1181. <https://doi.org/10.1109/28.62405>
- Chubb, J., & Harbour, J. (2000). *A system for the advance warning of risk of lightning*. Paper presented at the Electrostatics Society of America 'ESA 2000' meeting Niagara Falls June 18–21 2000. Retrieved from <http://www.infostatic.co.uk/Papers/ESA-Lightning.pdf>
- Cizek, V. (1970). Discrete hilbert transform. *IEEE Transactions on Audio and Electroacoustics*, *18*(4), 340–343. <https://doi.org/10.1109/tau.1970.1162139>
- de Boor, C. (1978). *A practical guide to splines*. New York: Springer.

Acknowledgments

This research was supported by NSF grant AGS 1661726, and the CU EFM invention is protected under patent application no. 62/835,817. A. A. is supported by a NASA Earth and Space Science Fellowship, grant number 80NSSC17K0392. We thank Mr. Connor Myers for help with the manufacturing of the first-gen field mills deployed in RELAMPAGO. We also thank Earth Networks for providing access to the ENTLN data set during RELAMPAGO.

- Deierling, W., Marshall, R., Sá, A., & Sousa, A. (2019). CU electric field mill data. Version 1.0. UCAR/NCAR - Earth Observing Laboratory <https://data.eol.ucar.edu/dataset/553.035>
- Earth Networks (2020). Earth networks lightning network. <https://www.earthnetworks.com/why-us/networks/lightning/>
- Harnwell, G. P., & Voorhis, S. N. V. (1933). An electrostatic generating voltmeter. *Review of Scientific Instruments*, 4(10), 540–541. <https://doi.org/10.1063/1.1748995>
- Harrison, R. G. (2012). The carnegie curve. *Surveys in Geophysics*, 34(2), 209–232. <https://doi.org/10.1007/s10712-012-9210-2>
- Horenstein, M. N., & Stone, P. R. (2001). A micro-aperture electrostatic field mill based on MEMS technology. *Journal of Electrostatics*, 51–52, 515–521. [https://doi.org/10.1016/s0304-3886\(01\)00048-1](https://doi.org/10.1016/s0304-3886(01)00048-1)
- IEEE Standard 1227-1990 (1990). IEEE guide for the measurement of DC electric-field strength and ion related quantities. IEEE <https://doi.org/10.1109/ieeestd.1990.101059>
- Jacobson, E. A., & Krider, E. P. (1976). Electrostatic field changes produced by Florida lightning. *Journal of the Atmospheric Sciences*, 33(1), 103–117. [https://doi.org/10.1175/1520-0469\(1976\)033<0103:efcpbf>2.0.co;2](https://doi.org/10.1175/1520-0469(1976)033<0103:efcpbf>2.0.co;2)
- Koshak, W. J., & Krider, E. P. (1989). Analysis of lightning field changes during active Florida thunderstorms. *Journal of Geophysical Research*, 94(D1), 1165. <https://doi.org/10.1029/JD094id01p01165>
- Koshak, W. J., & Krider, E. P. (1994). A linear method for analyzing lightning field changes. *Journal of the Atmospheric Sciences*, 51(4), 473–488. [https://doi.org/10.1175/1520-0469\(1994\)051<0473:almfal>2.0.co;2](https://doi.org/10.1175/1520-0469(1994)051<0473:almfal>2.0.co;2)
- Lang, T. (2020). Remote sensing of electrification, lightning, and mesoscale/microscale processes with adaptive ground observations (relampago) Lightning Mapper Array (LMA). NASA Global Hydrology Resource Center DAAC. <https://doi.org/10.5067/RELAMPAGO/LMA/DATA101>
- Liu, C., Williams, E. R., Zipser, E. J., & Burns, G. (2010). Diurnal variations of global thunderstorms and electrified shower clouds and their contribution to the global electrical circuit. *Journal of the Atmospheric Sciences*, 67(2), 309–323. <https://doi.org/10.1175/2009jas3248.1>
- Lucas, G. M., Thayer, J. P., & Deierling, W. (2017). Statistical analysis of spatial and temporal variations in atmospheric electric fields from a regional array of field mills. *Journal of Geophysical Research: Atmospheres*, 122, 1158–1174. <https://doi.org/10.1002/2016JD025944>
- Mach, D. M., Blakeslee, R. J., & Bateman, M. G. (2011). Global electric circuit implications of combined aircraft storm electric current measurements and satellite-based diurnal lightning statistics. *Journal of Geophysical Research*, 116, D05201. <https://doi.org/10.1029/2010JD014462>
- Mach, D. M., Blakeslee, R. J., Bateman, M. G., & Bailey, J. C. (2010). Comparisons of total currents based on storm location, polarity, and flash rates derived from high-altitude aircraft overflights. *Journal of Geophysical Research*, 115, D03201. <https://doi.org/10.1029/2009JD012240>
- Maier, L. M., & Krider, E. P. (1986). The charges that are deposited by cloud-to-ground lightning in Florida. *Journal of Geophysical Research*, 91(D12), 13275. <https://doi.org/10.1029/JD091id12p13275>
- Malan, D. J., & Schonland, B. F. J. (1950). An electrostatic fluxmeter of short response-time for use in studies of transient field-changes. *Proceedings of the Physical Society. Section B*, 63(6), 402–408. <https://doi.org/10.1088/0370-1301/63/6/303>
- Mapleson, W. W., & Whitlock, W. S. (1955). Apparatus for the accurate and continuous measurement of the Earth's electric field. *Journal of Atmospheric and Terrestrial Physics*, 7, 61–72. [https://doi.org/10.1016/0021-9169\(55\)90107-0](https://doi.org/10.1016/0021-9169(55)90107-0)
- Markson, R. (2007). The global circuit intensity: Its measurement and variation over the last 50 years. *Bulletin of the American Meteorological Society*, 88(2), 223–242. <https://doi.org/10.1175/bams-88-2-223>
- Montanya, J., Bergas, J., & Hermoso, B. (2004). Electric field measurements at ground level as a basis for lightning hazard warning. *Journal of Electrostatics*, 60(2–4), 241–246. <https://doi.org/10.1016/j.elstat.2004.01.009>
- Murphy, M. J., Holle, R. L., & Demetriades, NWS (2008). Cloud-to-ground lightning warnings using electric field mill and lightning observations. In *20th International Lightning Detection Conference (ILDC)*. Tucson, USA.
- Murphy, M. J., Krider, E. P., & Maier, M. W. (1996). Lightning charge analyses in small convection and precipitation electrification (CaPE) experiment storms. *Journal of Geophysical Research*, 101(D23), 29,615–29,626. <https://doi.org/10.1029/96JD01538>
- NXP Semiconductors (2017). Kinetis K66 sub-family 180 MHz Arm Cortex-M4F Microcontroller. Computer software manual No. K66P144M180SF5V2 Rev. 4 <https://www.nxp.com/docs/en/data-sheet/K66P144M180SF5V2.pdf>
- Nesbitt, S. (2020). RELAMPAGO-CACTI. <https://sites.google.com/illinois.edu/relampago/home>
- Pellat, H. (1890). *Léçons sur l'Électricité (électrostatique, pile, électricité atmosphérique)* (p. 332). Paris.
- Renolfi, F., Salio, P., & Nesbitt, S. (2020). Cordoba (RMA1) radar data. Version 1.0. UCAR/NCAR—Earth Observing Laboratory. <https://doi.org/10.26023/TTK1-C4VG-VG0K>
- Roble, R., & Tzur, I. (1986). The global atmospheric electrical circuit, *The Earth's electrical environment* (pp. 206–231). Washington, DC: National Academies Press.
- Secker, P. E. (1975). The desing of simple instruments for measurement of charge on insulating surfaces. *Journal of Electrostatics*, 1(1), 27–36. [https://doi.org/10.1016/0304-3886\(75\)90005-4](https://doi.org/10.1016/0304-3886(75)90005-4)
- Whipple, F. J. W. (2007). Modern views on atmospheric electricity. *Quarterly Journal of the Royal Meteorological Society*, 64(275), 199–222. <https://doi.org/10.1002/qj.49706427502>
- Williams, E., & Mareev, E. (2014). Recent progress on the global electrical circuit. *Atmospheric Research*, 135–136, 208–227. <https://doi.org/10.1016/j.atmosres.2013.05.015>
- Winn, W. P., & Moore, C. B. (1971). Electric field measurements in thunderclouds using instrumented rockets. *Journal of Geophysical Research*, 76(21), 5003–5017. <https://doi.org/10.1029/JC076i021p05003>